The Astrophysical Journal, 985:188 (16pp), 2025 June 1 https://doi.org/10.3847/1538-4357/adceb4

Viewing Global Changes in the Heliosheath with IMAP's Energetic Neutral Atom Imagers

E. J. Zirnstein[1], J. Heerikhuisen[2], D. J. McComas[1], J. Bower[3], G. Clark[4], M. A. Dayeh[5], H. O. Funsten[6], M. Gkioulidou[4], D. G. Mitchell[4], D. B. Reisenfeld[6], and N. A. Schwadron[1,3]
[1] Department of Astrophysical Sciences, Princeton University, Princeton, NJ 08544, USA; ejz@princeton.edu
[2] Department of Mathematics and Statistics, University of Waikato, Hamilton, New Zealand
[3] Space Science Center, University of New Hampshire, Durham, NH 03824, USA
[4] Johns Hopkins University Applied Physics Laboratory, Laurel, MD 20723, USA
[5] Southwest Research Institute, San Antonio, TX 78228, USA
[6] Los Alamos National Laboratory, Los Alamos, NM 87545, USA

Received 2025 March 18; accepted 2025 April 18; published 2025 May 23

Abstract

We present a simulation analysis of NASA's upcoming Interstellar Mapping and Acceleration Probe (IMAP) energetic neutral atom (ENA) instrument capabilities in viewing "global" changes in the heliosheath (HS) plasma, and the resulting ENA flux changes detected near Earth. This is done by simulating ENA emissions produced by charge exchange in a simulated heliosphere, utilizing the instruments' energy coverage, and calculating the time it takes for the SW to travel from 1 au to the HS and for ENAs to travel back. We aim to answer the following: (i) What are the time delays as a function of energy and direction; (ii) at what energies can we observe changes the soonest; and (iii) what might the ENA source distributions affecting the time delays look like? We find the following: (i) The time delay depends on energy and direction in the sky, taking from >20 yr to <2 yr to see a response. The time delay does not decrease monotonically with increasing ENA energy, because of the energy-dependent, H+p charge exchange cross section. (ii) The quickest changes can be observed at ∼15 keV (without HS energy diffusion), intersecting IMAP-Hi and IMAP-Ultra energies. (iii) The ENA source distributions, and how far out IMAP can "see" the heliosphere, strongly depend on energy: IMAP-Lo and IMAP-Ultra should be able to view the farthest back in the heliotail but with long delay times. Finally, we show how energy diffusion in the HS affects the time delays and ENA source distributions, increasing ENA fluxes and prolonging time delays.

Unified Astronomy Thesaurus concepts: Heliosphere (711); Solar wind (1534); Solar wind termination (1535); Space plasmas (1544); Pickup ions (1239); Solar activity (1475); Ion-neutral reactions (2263)

1. Introduction

The heliosphere surrounding our solar system is formed by the interaction between the solar wind (SW) and the partially ionized, local interstellar medium (LISM; E. N. Parker 1961; V. B. Baranov & Y. G. Malama 1993; G. P. Zank 1999, 2015; D. J. McComas et al. 2009a). The interstellar plasma, consisting mostly of H and He, is slowed by the bow wave upstream of the heliosphere (D. J. McComas et al. 2012; G. P. Zank et al. 2013) and diverted around the heliopause boundary separating the solar and interstellar plasmas (D. A. Gurnett et al. 2013; J. D. Richardson et al. 2019; E. C. Stone et al. 2019, 2013). Interstellar neutral atoms, however, cross the heliopause and enter the heliosphere. Low-energy interstellar neutrals are detected directly by the Interstellar Boundary Explorer (IBEX; D. J. McComas et al. 2009b) near Earth (D. J. McComas et al. 2009a; E. Möbius et al. 2009), but also experience charge exchange with SW ions and energetic pickup ions (PUIs) in the supersonic SW and in the heliosheath (HS), creating energetic neutral atoms (ENAs) at much higher energies. The IBEX-Hi ENA imager (H. O. Funsten et al. 2009) can detect ENAs at energies up to ∼6 keV from all directions of the sky, and has accumulated more than 15 yr of ENA observations since its launch in late 2008 (D. J. McComas et al. 2020, 2024).

IBEX has operated successfully and made numerous discoveries over the past 15 yr (D. J. McComas et al. 2017, 2024; A. Galli et al. 2022). While it is expected to continue operating and taking measurements for the near future, a new NASA mission scheduled for launch in 2025, called the Interstellar Mapping and Acceleration Probe (IMAP; D. J. McComas et al. 2018a), will improve on IBEX's capabilities by measuring ENA fluxes over a larger energy range with greater angular, spectral, and temporal accuracy and precision. IMAP is equipped with three neutral atom imagers, IMAP-Lo, IMAP-Hi, and IMAP-Ultra, which will measure neutral atom fluxes from 5 eV to 1 keV, 0.4 keV to 16 keV, and 5 keV to 40 keV (and potentially up to $\gtrsim$100 keV, depending on the signal-to-noise ratio, SNR), respectively. IMAP-Lo and IMAP-Hi, both single-pixel ENA imagers, utilize electrostatic analyzers (ESAs) and time-of-flight (TOF) subsystems to measure neutral atom fluxes with greater SNRs than their IBEX predecessors. IMAP-Ultra comprises a large 90° × 120° field of view, charged-particle deflection plates, variable slit apertures, and a foil-based TOF and energy (solid-state detectors) subsystem to detect both neutral atom and ion particle fluxes. IMAP-Lo is mounted on a pivot platform, allowing it to view the inflowing interstellar neutral gas over a longer period of the year. IMAP-Hi and IMAP-Ultra are each comprised of two identical sensors with different look directions relative to the spacecraft spin axis, with the sensors viewing in the anti-sunward direction providing concentrated exposure of low ecliptic latitudes (<|±45°|). With their greater sensitivity, the IMAP ENA imagers will be able to produce full sky maps every 6 months and partial sky maps every ~3 months, allowing us to quantify variability in the outer heliosphere at twice the cadence of IBEX.

It has become clear over the past decade that the heliosphere responds on a global scale to abrupt changes in the SW dynamic pressure (D. J. McComas et al. 2018b). Voyager observations within the HS have shown large variability in the magnetic field and thermal ion properties and transients propagating across the HS and into the LISM (J. D. Richardson et al. 2017; J. S. Rankin et al. 2019; L. F. Burlaga et al. 2021), as well as the dynamic characteristics of the heliosphere boundaries (L. F. Burlaga et al. 2008; E. C. Stone et al. 2005, 2008, 2013, 2019; S. M. Krimigis et al. 2019; J. D. Richardson et al. 2019), but only along their respective spacecraft trajectories. IBEX-Hi, with its ability to map the entire sky every six months, has revealed long-term and gradual changes in ENA fluxes in the outer heliosphere (D. J. McComas et al. 2017, 2020; N. A. Schwadron et al. 2018; E. J. Zirnstein et al. 2020a), as well as short-term and abrupt variability directly caused by SW pressure changes (D. J. McComas et al. 2018b, 2019; E. J. Zirnstein et al. 2018a; D. B. Reisenfeld et al. 2021). The large increase in SW dynamic pressure observed by ACE and Wind in late 2014 at 1 au was reflected in enhanced ENA emissions measured by IBEX beginning in late 2016 (D. J. McComas et al. 2018b). Strong changes in SW pressure such as this reveal the asymmetric shape of the heliosphere via the time delays present in ENA emissions from different directions of the sky (E. J. Zirnstein et al. 2018a; McComas et al. 2020; D. B. Reisenfeld et al. 2021). These large pressure increases appear to have occurred over the last several solar cycles (J. M. Sokół et al. 2021).

With the upcoming launch of NASA's IMAP mission, it is of great importance that the heliospheric community has a better grasp on how the IMAP ENA imagers can be used to detect and correlate large-scale changes in the SW with ENA emissions across the sky. D. B. Reisenfeld et al. (2021) and E. J. Zirnstein et al. (2022b) demonstrated how IBEX measurements can be used to map the heliospheric structure using in situ measurements of the SW dynamic pressure. However, there are limitations to this approach: the energy's range and the resolution at which the ENA imagers take these measurements. IBEX-Hi measurements, for example, are limited to ~0.5–6 keV, and therefore we can only "observe" a limited distance down the heliotail due to the "cooling length" effect (N. A. Schwadron et al. 2011, 2014; A. Galli et al. 2017; E. J. Zirnstein et al. 2017, 2020b; M. Kornbleuth et al. 2023); at higher energies (>20 keV), the number of ENAs is significantly depleted by a steep drop in the charge-exchange cross section (B. G. Lindsay & R. F. Stebbings 2005). This hindrance is mitigated by the capabilities of the IMAP ENA imagers, in particular IMAP-Hi and IMAP-Ultra, which have significantly higher energy ranges.

Considering these improvements in IMAP, this study presents a simulation of the heliosphere where we create all-sky maps that quantify the "time delay" between SW observed at 1 au, its propagation and processing in the outer heliosphere, and its return via ENAs and measurement at IMAP in each direction of the sky, for each ENA imager and energy. This study investigates the time delays induced by large changes in SW dynamic pressure for a range of energies from ~0.06 to 100 keV, how soon changes in the SW (such as the abrupt increase in SW dynamic pressure in late 2014; D. J. McComas et al. 2018b, 2019; E. J. Zirnstein et al. 2018a) that affect the heliosphere can be observed by IMAP, and how the size and properties of the ENA source plasmas affect these time delays as a function of ENA energy. Finally, we test a model of proton energization in the HS to see how energy diffusion can both increase and decrease the ENA source distributions and affect the SW-to-ENA detection delay times.

2. Methodology

2.1. Instrument Response Functions

We summarize below the energy response functions for each IMAP ENA imager used in the simulations. These response functions are derived from a combination of lab calibration data and models of the imagers' response functions provided by the IMAP ENA instrument teams.

2.1.1. IMAP-Lo

The IMAP-Lo energy response ($R_{\mathrm{IMAP-Lo}}$) functions are derived from the current IMAP-Lo end-to-end performance model over multiple energy passbands. The best-fit model to the simulated response data is a Gaussian distribution with a full width at half maximum (FWHM) of $(dE/E)_c \cong 1.0$, where E_c is the central energy of the passband. The set of equations that define the energy response function is given as

$$R_{\mathrm{IMAP-Lo}}(E_c, E) \propto \exp[-(E-\mu)^2/(2\sigma^2)], \tag{1}$$

$$\mu = E_c, \tag{2}$$

$$\sigma^2 = \{(dE/E)_c \times E_c/[2\sqrt{2\ln(2)}]\}^2. \tag{3}$$

The specific central energies and FWHM for IMAP-Lo energy passbands we consider here are shown in Table 1.

2.1.2. IMAP-Hi

The IMAP-Hi energy response ($R_{\mathrm{IMAP-Hi}}$) functions are derived from the current IMAP-Hi end-to-end performance model. The energy response function is approximately log-Gaussian, with FWHM close to $(dE/E)_c \sim 0.4$ at central energies ranging from 0.5 to 12.7 keV. The equations defining the log-Gaussian response function are as follows:

$$R_{\mathrm{IMAP-Hi}}(E_c, E) \propto \exp[-(\ln(E)-\mu)^2/(2\sigma^2)]/E, \tag{4}$$

$$\mu = \ln[\eta/\sqrt{1+\nu^2}], \tag{5}$$

$$\sigma^2 = \ln[1+\nu^2], \tag{6}$$

$$\eta = E_c\Gamma, \tag{7}$$

$$\nu = (dE/E)_c/[2\sqrt{2\ln(2)}], \tag{8}$$

$$\Gamma = (1+\nu^2)^{3/2}. \tag{9}$$

Table 1 shows the central energies and FWHM of IMAP-Hi's energy passbands.

2.1.3. IMAP-Ultra

Unlike the other two instruments that utilize ESAs, IMAP-Ultra is a slit-based imager that measures the TOF and mass of individual neutral particles entering the aperture. IMAP-Ultra achieves an energy resolution of $(dE/E)_c \leqslant 0.12$ per particle for $E_c > 10$ keV. We note that, to achieve a high enough SNR for studies of temporal variations of ENA flux over time, fluxes

Table 1
IMAP ENA Imagers Energy Information Used in This Study

	IMAP-Lo		IMAP-Hi		IMAP-Ultra	
	Passbands 3–7[a]		Passbands 1–9[b]		Bins 1–10[c]	
Energy Step	Central Energy (keV)	dE/E_c	Central Energy (keV)	dE/E_c	Central Energy (keV)	dE/E_c
1	(0.0165)[a]	(1.01)[a]	0.50	0.40	10.0	0.40
2	(0.0322)[a]	(1.01)[a]	0.75	0.42	12.9	0.40
3	0.0626	1.01	1.13	0.42	16.7	0.40
4	0.123	1.02	1.68	0.42	21.5	0.40
5	0.241	1.03	2.52	0.40	27.8	0.40
6	0.496	1.04	3.75	0.41	35.9	0.40
7	0.969	1.03	5.62	0.40	46.4	0.40
8	…	…	8.42	0.39	59.9	0.40
9	…	…	12.7	0.40	77.4	0.40
10	…	…	…	…	100.0	0.40

Notes.

[a] IMAP-Lo's energy response function is well approximated by a Gaussian distribution based on lab calibration measurements. We do not simulate energies below ∼60 eV, and thus we only include passbands 3 and above for IMAP-Lo.

[b] IMAP-Hi's energy response function is well approximated by a log-Gaussian distribution based on lab calibration measurements.

[c] IMAP-Ultra uses a TOF mass spectrometer instead of an ESA; therefore, we constructed 10 energy bins spaced out logarithmically from 10 keV to 100 keV, where the SNR is expected to be ∼2 with $dE/E_c = 0.40$ at ∼100 keV. We assume the counts are uniformly weighted in each bin. See Section 2.1.5 for more details.

observed by IMAP-Ultra will need to be combined over a range of energies. An initial trade study suggests that, to perform studies of temporal variations at a <12 month cadence, fluxes likely need to be binned over energy ranges with FWHM $(dE/E)_c \sim 0.4$ to obtain an SNR of ∼2 at $E_c \sim 100$ keV, and SNRs of ∼90 or ∼60 at $E_c \sim 10$ keV for the "Belt" and "Basin" regions in the sky, respectively (see K. Dialynas et al. 2022 and references therein for more information on the Belt and Basin regions observed by Cassini-INCA). It is simplest to assume that binning fluxes over energy will be uniform in weighting, such that the effective energy response of IMAP-Ultra for our analysis is $(dE/E)_c = 0.4$ with uniform weighting. Because IMAP-Ultra does not use ESAs to define an energy passband, we are free to construct 10 binned energy ranges, logarithmically spaced from 10 keV to 100 keV (see Table 1). For the purposes of this paper, we do not simulate energies above 100 keV, where fluxes are expected to be extremely low.

2.2. Simulation of the Heliosphere and Energetic Neutral Atoms

We utilize output from a global magnetohydrodynamic (MHD)/kinetic simulation of the solar–interstellar interaction (E. J. Zirnstein et al. 2022b, 2025). The simulation grid has 764 × 120 × 180 cells in spherical coordinates (r, θ, ϕ), respectively. The radial grid extends from an inner boundary at 10 au to an outer boundary at 2500 au, with radial resolution of $\Delta r \sim 0.7$ au at 50 au, $\Delta r \sim 1.3$ au at 200 au, $\Delta r \sim 2.4$ au at 500 au, and $\Delta r \sim 8$ au at 2000 au. The angular resolution is $1\overset{\circ}{.}5$ for θ and 2° for ϕ. The simulation solves the single-fluid MHD equations with photoionization and charge-exchange source terms, where the source terms are coupled to neutral H atoms traversing the simulation domain, which are solved using Boltzmann's equation (see, e.g., J. Heerikhuisen et al. 2006, J. Heerikhuisen & N. V. Pogorelov 2010, E. J. Zirnstein et al. 2015 and references therein).

The inner SW boundary conditions are defined at 1 au and then adiabatically expanded to the simulation's inner boundary at 10 au. At low latitudes (slow SW, from the OMNI database averaged over 2004–2009), the SW speed = 449 km s^{-1}, density = 6.53 cm^{-3}, temperature = 1.05×10^5 K, and radial magnetic field = 37.4 μG, solved assuming a Parker spiral with a 45° transverse angle at 1 au. At high latitudes (fast SW, from Ulysses' third polar scan in 2007), the inner boundary conditions are speed = 743 km s^{-1}, density = 2.23 cm^{-3}, temperature = 2.98×10^5 K, and radial magnetic field = 34.7 μG. The latitude at which the slow SW transitions to fast SW is $\pm 37\overset{\circ}{.}5$.

The outer LISM boundary conditions are defined at 2500 au from the Sun, where the properties are determined from a combination of IBEX ENA and New Horizons' SWAP PUI observations. The LISM flow speed = 25.4 km s^{-1} (D. J. McComas et al. 2015). The total effective plasma density = 0.09 cm^{-3}, where the interstellar proton density is ∼60% or 0.054 cm^{-3}, and the remainder is interstellar He$^+$ with density = 0.009 cm^{-3} but four times the mass as protons, such that $0.054\ \mathrm{cm}^{-3} + 4 \times 0.009\ \mathrm{cm}^{-3} = 0.09\ \mathrm{cm}^{-3}$ (M. Bzowski et al. 2019). Note that, in the MHD/Boltzmann charge-exchange source terms, the plasma is comprised of a single-fluid mixture of protons and He$^+$, thus approximating the presence of interstellar He$^+$ through charge exchange, and they are assumed to be comoving. The neutral H density = 0.17 cm^{-3}, the temperature for both plasma and neutrals = 7500 K (D. J. McComas et al. 2015), the magnetic field strength = 2.93 μG, and the orientation is $(227\overset{\circ}{.}28, 34\overset{\circ}{.}62)$ in ecliptic J2000 (E. J. Zirnstein et al. 2016). The neutral H density is chosen such that the filtration of interstellar neutral H through the front of the simulated heliosphere yields H densities consistent with New Horizons' SWAP (D. McComas et al. 2008) observations near 40 au from the Sun (P. Swaczyna et al. 2020, 2024). This requirement, along with the standoff distance of the heliopause, gives the proton density needed to achieve the right amount of neutral filtration. Because the thickness of our simulated HS is larger than what is inferred from the observations—the simulated thickness is ∼45 au rather than ∼30–35 au from Voyager observations (D. A. Gurnett et al. 2013; E. C. Stone et al. 2013, 2019; L. F. Burlaga et al. 2019, 2013; J. D. Richardson et al. 2019), the LISM plasma and neutral densities are adjusted until the distance to the middle of the HS in the Voyager directions agrees with Voyager observations of where the middle of the HS is. We simulate the proton distribution in the HS by solving the Parker transport equation with photoionization and charge-exchange source terms, as shown in Equation (13) in the Appendix. We first assume in Sections 3.1 and 3.2 that the diffusion coefficient $D = 0$, i.e., there is no energy diffusion. In Section 3.3, we allow $D > 0$ and show how energy diffusion in the HS affects the results.

3. Simulation Results

3.1. ENA Source Distance and Total Time Delays

The cumulative time delay, T_{tot}, is calculated by adding the time it takes for the simulated SW plasma to propagate from 1 au to the termination shock, the time it takes the SW plasma to propagate along multiple flow streamlines to a point in the HS that intersects the desired line-of-sight (LOS) direction (i.e., a 2° × 2° pixel in the sky) as viewed by an IMAP ENA imager, and the normalized, flux-weighted averaged time it takes ENAs at the desired energy to travel from their creation points via charge exchange along the LOS back to 1 au. Effectively, this is done by (1) integrating the ENA backward in time along the desired IMAP LOS from 1 au to the termination shock, (2) taking small steps along the LOS through the HS, where at each step we trace back along the HS flow streamline to the termination shock to find the time it takes the HS plasma to flow there, and then (3) integrating the time it takes for the SW to go from the shock back to 1 au along each of those streamlines. The streamlines that connect to the desired LOS that produce a higher proton flux yield a higher weight for the time delay (i.e., the local proton flux is the weight). This can be quantified as

$$T_{\rm tot}(E_j, \Omega) = T^{\rm ENA}_{1{\rm au}-to-TS} + \frac{1}{\sum_{i=1}^{N} w_i} \sum_{i=1}^{N} w_i \times \left(T^{\rm ENA}_{{\rm TS}-to-r_i} + T^{\rm SW}_{r_i-to-TS_i} + T^{\rm SW}_{{\rm TS}_i-to-1{\rm au}}\right), \quad (10)$$

where E_j is the desired ENA energy, Ω is the desired LOS direction, and $w_i = J_i^p(E', \boldsymbol{r})$ is the proton flux weight at desired energy E' in the plasma frame and position $\boldsymbol{r}$ along the LOS. The sums in Equation (10) represent the integration over multiple streamlines N, each producing ENAs over some increment i to i+1 along the LOS, with their own weight w_i. The procedure is repeated for different energies E_j within the energy passband/bin and weighted by the ENA imager's ESA response function (or uniform binning for IMAP-Ultra).

Figure 1 shows example sky maps of the total SW-to-ENA time delay for each IMAP ENA imager. Note that, while we say "SW," the ENAs we observe are predominantly from PUIs that are comoving with the SW. The time delays range from <2 yr to >20 yr, depending on the energy and direction in the sky. The longest delay times occur at the lowest energies, due in part to the ENA travel time but also to the plasma flow time (this will be explained next). As energy increases, the delay time decreases. However, this behavior is not monotonic. At energies above ∼20 keV, the total time delay begins to increase again, especially in the heliotail, due to the increased path length to the ENA source.

Figure 2 shows the mean distances to the ENA source for the upwind, downwind, port, starboard, north pole, and south pole directions (all in ecliptic J2000 coordinates). These distances are calculated similarly to the time delays, with weights equal to the local proton flux. We show distances as measured by each ENA imager, from ∼0.06 to 100 keV. The energies and passband/binning information simulated in this study are shown in Table 1. As one can see, there is an energy dependence to the ENA source distance, especially from the downwind direction. There are also clear asymmetries between the port versus starboard directions, as well as the north versus south pole directions. Note that the shaded regions in Figures 2 and 3 represent the ±1σ standard errors of the weighted means, which are calculated as

$$\bar{X} = \frac{\sum_{i=1}^{N} w_i X_i}{\sum_{i=1}^{N} w_i}, \quad (11)$$

$$\sigma_X = \sqrt{\frac{N}{N-1} \frac{\sum_{i=1}^{N} w_i (\bar{X} - X_i)^2}{\sum_{i=1}^{N} w_i}} \times \sqrt{\frac{\sum_{i=1}^{N} w_i^2}{\left(\sum_{i=1}^{N} w_i\right)^2}} \cong \sqrt{\frac{\sum_{i=0}^{N} w_i (\bar{X} - X_i)^2}{\sum_{i=0}^{N} w_i} \frac{\sum_{i=1}^{N} w_i^2}{\left(\sum_{i=1}^{N} w_i\right)^2}}, \quad (12)$$

where X is the distance (Figure 2) or time delay (Figure 3) variable, N is the number of nonzero values, w is the weight (the local proton flux), $\bar{X}$ is the weighted mean, and σ_X is the standard error of the weighted mean. Here, we know that $N \gg 1$ in our simulation, and thus the approximation in Equation (12) is valid.

Similar behavior in the total time delays is shown in Figure 3. The longest distance, and longest time delay, occurs at the lowest of IMAP-Lo energies, as well as the highest energies for IMAP-Ultra. There is a local minimum around ∼15 keV in each panel of Figure 3. The reason for this behavior is the energy-dependent, H+p charge-exchange cross section (B. G. Lindsay & R. F. Stebbings 2005). Figure 4 shows the H+p charge-exchange cross section multiplied by the speed of interaction, as a function of interaction energy. There is a local maximum near ∼15–20 keV, then a significantly steep drop at higher energies, and a shallower drop at lower energies. The drop in the cross section at high energies means that fewer ENAs are created at these energies, and thus more energetic protons survive in the HS at larger distances from the termination shock. This means the effective distance to the ENA source has increased, and the time it takes for the SW and ENAs to travel that distance is longer. This effect competes with the cooling length effect, where ∼1–6 keV particles are especially susceptible to charge exchange in the HS, yielding source distributions that do not extend far down the heliotail. Figure 3 not only shows the total delay time (solid curve), but also the total ENA (dashed curve) and plasma (dotted curve) travel times. Typically, the plasma travel time (ions traveling at the bulk plasma flow speed) significantly exceeds the ENA travel time for ENA energies above 0.5 keV. This is especially true for IMAP-Ultra energies where the ENA travel time decreases with increasing energy to very small ENA delay times. The plasma, and thus total, delay time increases because the ENA source moves farther out and either closer to the heliopause or far down the heliotail, where the plasma flow speeds are small and the travel times are long.

As a side note, the H+p charge-exchange reaction is not the only important reaction to produce H ENAs. At ∼30 keV, the He+p charge-exchange reaction becomes equally important, and it is also included in our methodology. This can be seen in, for example, Figures 2 and 3 of K. Scherer et al. (2014). Because the density of interstellar neutral He is nonnegligible and the reaction rate is faster at the highest energies we simulate, it is important to include for studies of the high-energy portion of IMAP-Ultra observations. We use the Chebyshev polynomial fit from C. F. Barnett et al. (1990) to calculate the He+p charge-exchange reaction, where we assume the interstellar neutral He density is 0.015 cm^{-3} (M. Witte 2004) in the HS. Finally, recent updates have been made to the H+p reaction at energies <1 keV, from P. Swaczyna et al. (2019) and M. Bzowski & J. Heerikhuisen (2020); however, we use the cross section from B. G. Lindsay & R. F. Stebbings (2005), which is a good approximation for energies >1 keV and only exhibits <20% deviation from these two new models of the cross section for energies between 0.1 keV and 1 keV.

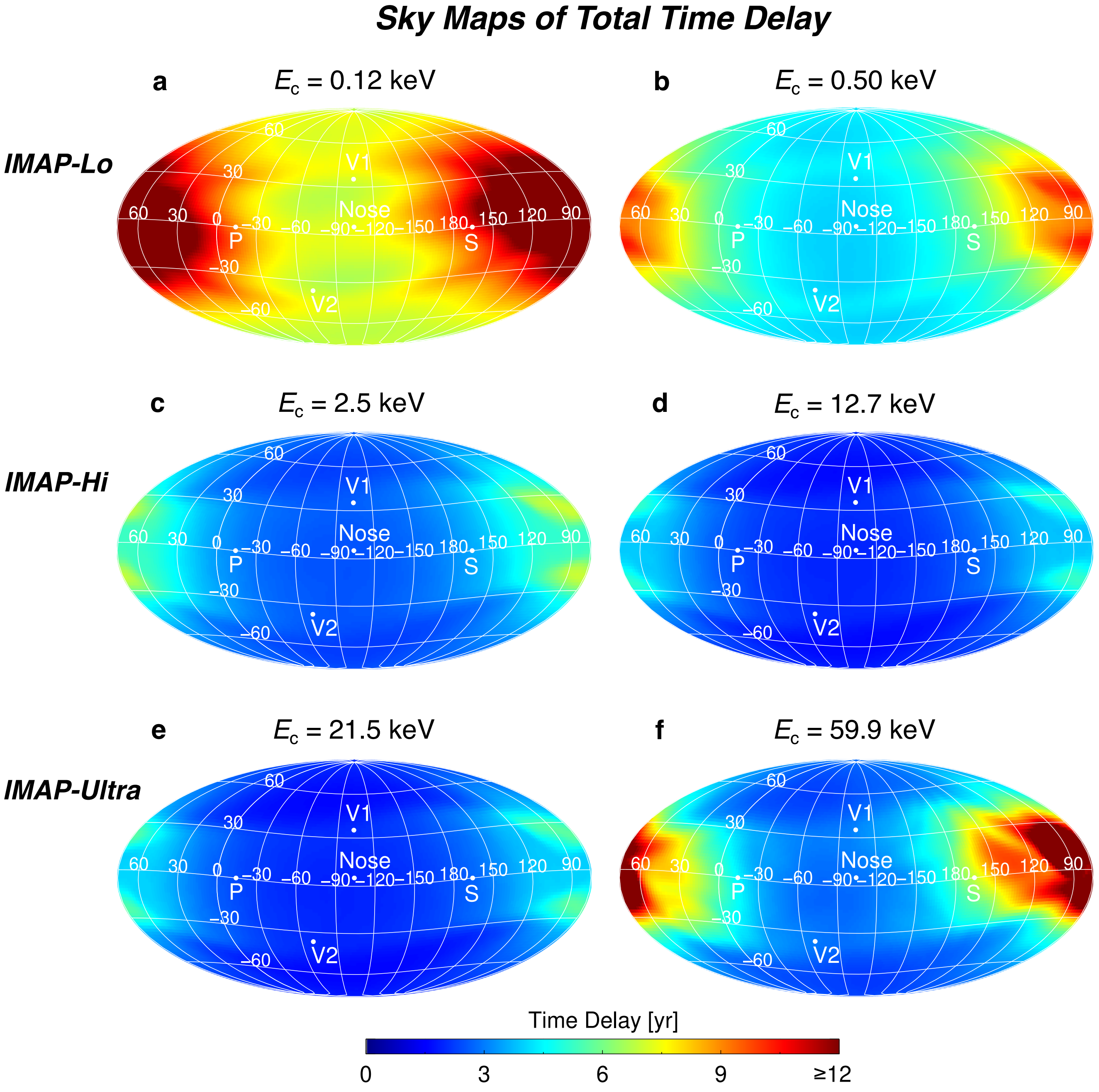

Figure 1. Example sky maps of the time delay between SW passing 1 au and ENA detection by IMAP, for (panels (a) and (b)) IMAP-Lo, (panels (c) and (d)) IMAP-Hi, and (panels (e) and (f)) IMAP-Ultra energies.

Returning to Figure 3, we can glean some interesting information from the time versus ENA energy behavior. As stated earlier, there is a minimum delay time for each pixel in the sky, largely determined by the ENA energy and charge-exchange cross section, and slightly by the direction in the sky. It may be a significant point of interest to focus on studying changes in the sky with IMAP where we know at what energies the quickest return times are expected to occur. Therefore, we calculated the minimum delay time for each pixel in the sky by fitting a third-order polynomial to the total delay times in log-energy over a limited range of energies (3.75–12.7 keV for IMAP-Hi and 16.7–46.4 keV for IMAP-Ultra, spanning a total range of 3.75–46.4 keV). We found the minimum of the polynomial within an accuracy of <0.1 keV. The results are shown in Figure 5.

Figure 5(a) shows a sky map of the minimum delay time (or fastest response possible) with the IMAP ENA imagers. Not surprisingly, the smallest delay times are in the noseward hemisphere of the heliosphere, and at high latitudes where the fast SW propagates from the polar coronal holes. Note that this is because our model of the heliosphere is a steady-state simulation of solar minimum-like conditions, so only fast SW propagates at high latitudes. Figure 5(b) shows the corresponding energy at which the minimum delay times can be observed. Over the whole sky, the energies are narrowly focused around $\sim$15 keV, where the cross section times speed of interaction reaches its peak. Generally, Figure 5(b) displays higher energies where the minimum delay time is smaller, and vice versa, except for some small regions in the sky. The reason for this can be understood by looking again at Figure 3. In the

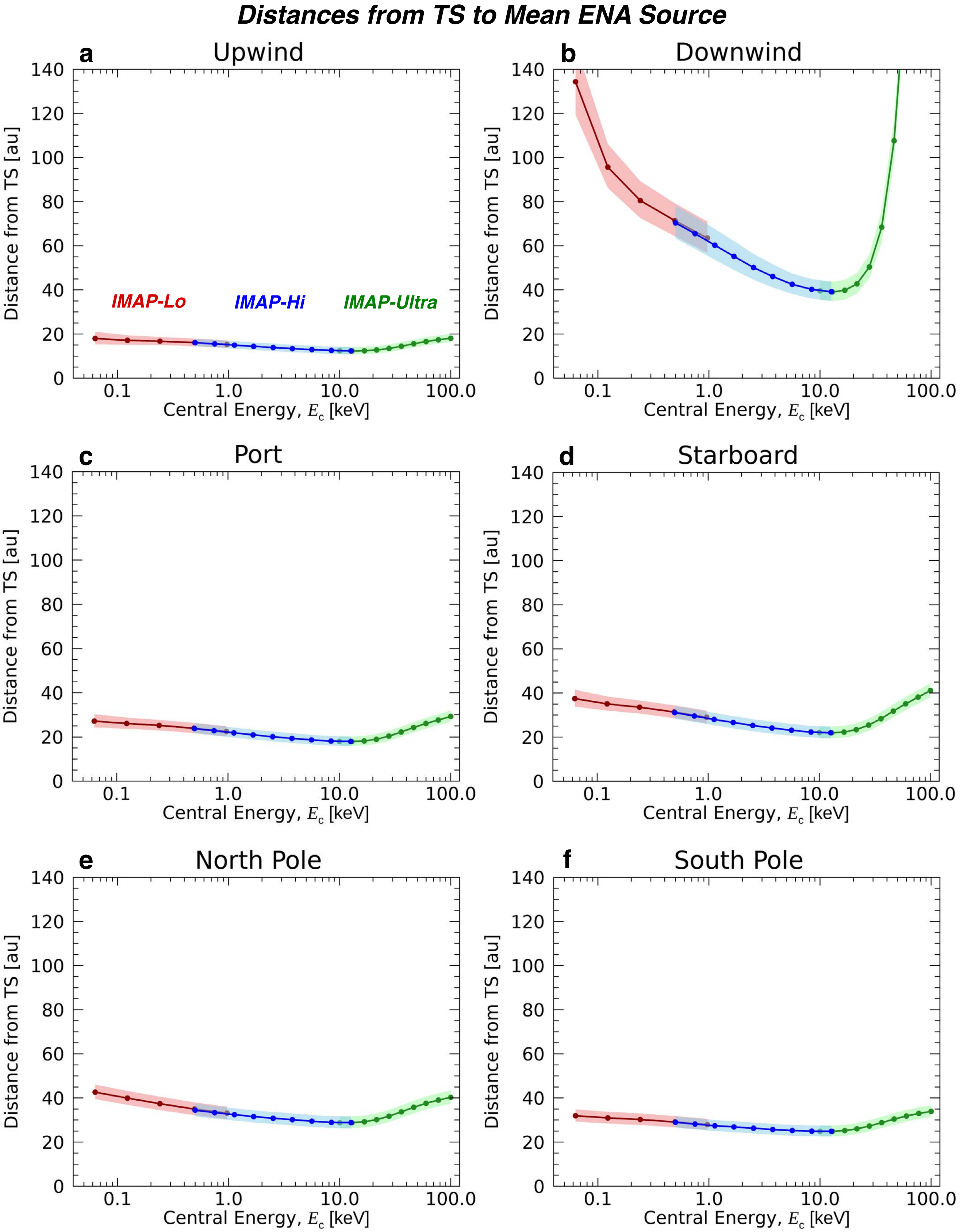

Figure 2. Plots of the mean distance from the TS to the ENA source as a function of ENA energy for each IMAP ENA imager. Shown are distances from the (a) upwind, (b) downwind, (c) port, (d) starboard, (e) north pole, and (f) south pole directions. The shaded regions indicate the standard error of the mean source.

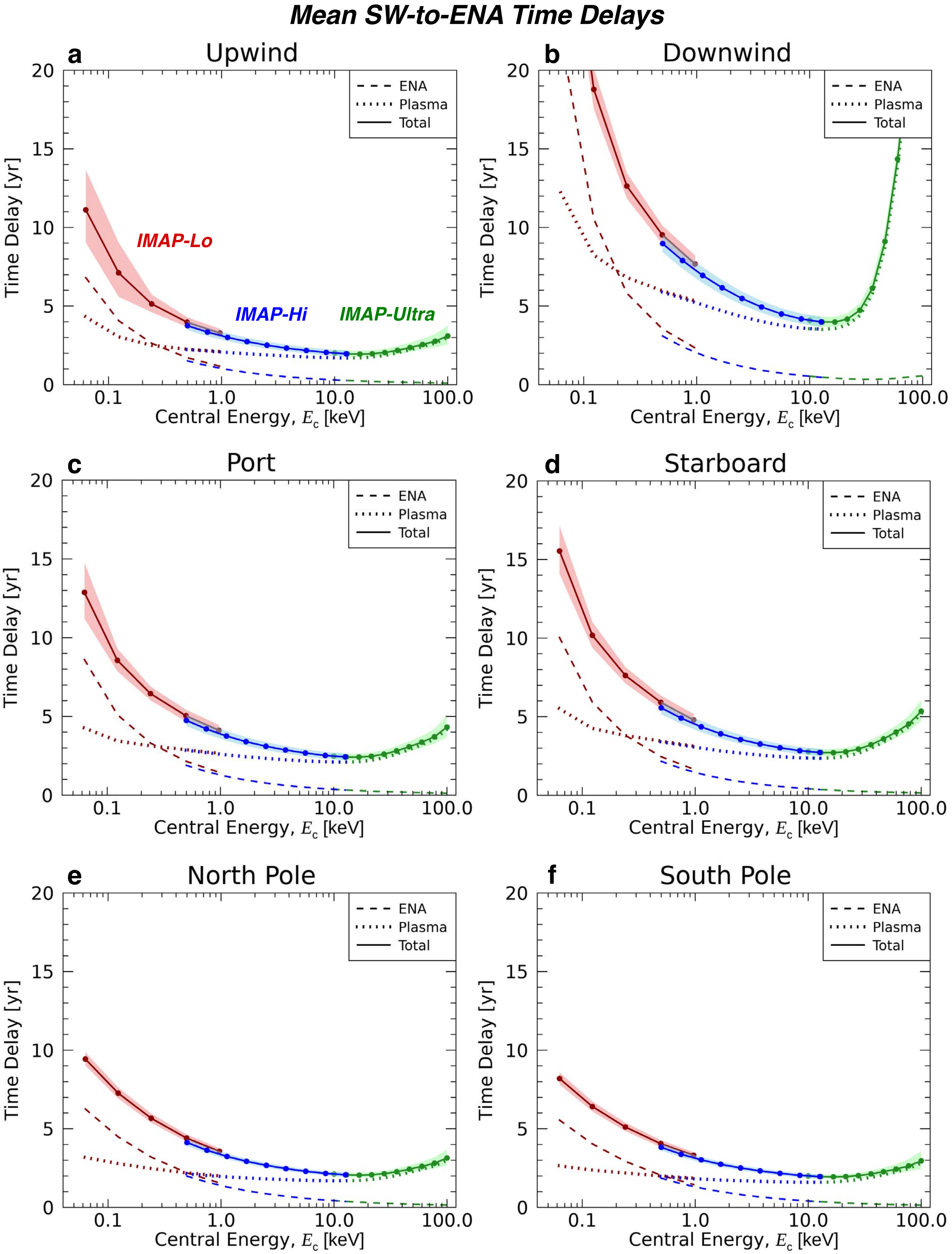

Figure 3. Time delay plots as a function of ENA energy for each IMAP ENA imager. Shown are time delays from the (a) upwind, (b) downwind, (c) port, (d) starboard, (e) north pole, and (f) south pole directions. The shaded regions indicate the standard error of the mean delay time (note that the error includes the spread of the ENA source distribution). In each panel, the energy ranges for IMAP-Lo, IMAP-Hi, and IMAP-Ultra are shown for different variables: (1) the total time delay (solid curve), (2) the plasma travel-time component (dotted curve), and the ENA travel-time component (dashed curve).

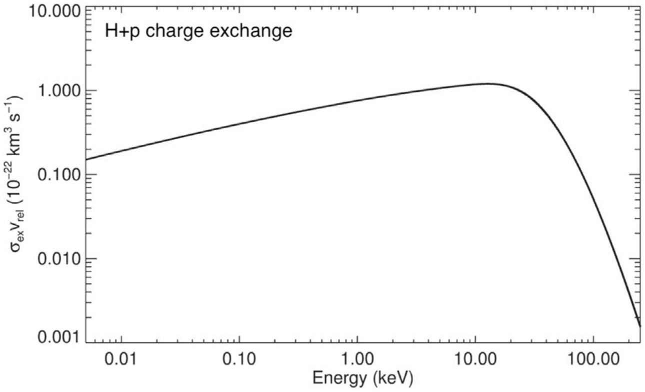

Figure 4. H+p charge-exchange reaction rate as a function of interaction energy. Adapted from E. J. Zirnstein & D. J. McComas (2015) with permission from AAS.

upwind versus downwind directions, for example, the steep rise in time delay for IMAP-Ultra above 30 keV, due to the drop in the charge-exchange cross section, pushes the minimum time delay to slightly lower energies (see also Figure 5(c)).

Because the steady-state assumption can be misleading at high latitudes, in particular in the heliotail, without the time-dependent history of fast and slow SW over multiple solar cycles (see, e.g., Figure 3 in E. J. Zirnstein et al. 2015), we show the in-ecliptic results from Figures 5(a) and (b) in Figure 5(c). This mimics the behavior seen in the previous panels at low latitudes, where the minimum delay time and energy at which it can be observed are approximately anticorrelated with each other.

3.2. ENA Source Distributions

The interstellar magnetic field squeezes and distorts the heliotail (D. J. McComas et al. 2013; J. Heerikhuisen et al. 2014), resulting in substantial complexity of the spatial extent and intensity of the 3D ENA source distributions. Despite this complexity, we can illustrate key findings using two orthogonal cross-sectional slices (solar meridional and equatorial planes) through the source distributions and bounded by 800 au in the tailward direction. Figures 6–8 show the ENA source distribution as a function of energy for each IMAP ENA imager. We note again that these results assume no energy diffusion ($D = 0$) in the HS. This assumption is relaxed in Section 3.3. Figure 6 illustrates cross-sectional slices of the ENA source distributions at central energies 0.12, 0.24, and 0.5 keV. These color plots are similar to those calculated in a prior study (E. J. Zirnstein et al. 2017), where integrating the local intensity along a LOS from 1 au to the heliopause gives the total ENA intensity observed at 1 au, for that specific energy passband/bin. At the lowest energy (0.12 keV; Figures 6(a) and (b)), the ENA source can be seen down the low-latitude heliotail for at least 400 au from the Sun, and as can be seen in Figure 6(a), perhaps even farther, i.e., to ∼700 au. Although not shown, at even lower energies, the ENA intensity becomes even higher far from the Sun. The reason for this is that the cooling length of very-low-energy ENAs is larger than, e.g., ∼1–6 keV particles, due to the drop in the H-H+ charge-exchange cross section as the interaction energy decreases (B. G. Lindsay & R. F. Stebbings 2005). This will allow IMAP-Lo to see farther down the tail at ∼100 eV. As we slowly increase the observable energy passband (Figures 6(c)–(f)), the ENA intensity decreases at low latitudes past 400 au from the Sun but begins to increase at high latitudes in the fast SW. Figures 6(d) and (f) clearly show, however, that the low-latitude intensity almost completely disappears by 400 au down the heliotail.

Figure 7 shows the ENA source distribution for IMAP-Hi central energies 0.5 keV, 2.5 keV, and 12.7 keV. The ENA source intensity begins to grow close to the termination shock but decreases at larger distances as the proton survival probability continues to decrease with time as the plasma propagates through the HS. At the passband with a central energy of 2.5 keV (Figures 7(c) and (d)), it is becoming clear that the main source of ENAs, besides directly upstream near the termination shock, is in the high-latitude, fast-SW plasma propagating down the heliotail.

Interestingly, Figure 8 (IMAP-Ultra at central energies 21.5 keV, 59.9 keV, and 100 keV) shows a reversal of the behavior seen in Figure 7—an increase in ENA production as energy increases. First, though, at the energy bin centered on 21.5 keV (Figures 8(a) and (b)), the source distribution looks rather similar to IMAP-Hi’s results at 12.7 keV. Between these energies is where the “peak” in the charge-exchange reaction rate occurs (see Figure 4). Therefore, we expect to see similar source distributions and time delays between ∼10 and 20 keV, though we note that the source intensity is about a factor of ∼3–4 lower at 21.5 keV. At higher energies (energy bin centered on 59.9 keV; Figures 8(c) and (d)), the ENA source distribution changes significantly. Besides an expected decrease in the overall intensity, the source is much more widely distributed in the HS than at lower energies, especially in the fast/hot SW. In the ecliptic plane, however, the source only extends to about ∼300 au from the Sun; thus, ENAs at ∼60 keV are much more sensitive to hotter plasma. Finally, at the energy bin centered at 100 keV (Figures 8(e) and (f)), the ENA source reaches nearly all the way to the heliopause in both cross sections of the heliosphere. We note again that these simulations assumed there is no energy diffusion in the HS; we relax this assumption in Section 3.3.

3.3. Effects of Proton Energy Diffusion in the Heliosheath

Next, we introduce energy diffusion in the HS following the procedure from E. J. Zirnstein et al. (2018b, 2018c, 2025), setting $D > 0$. To summarize the methodology, we solve the Parker transport equation with charge-exchange source terms, where advection with the MHD plasma flow, energy diffusion, and adiabatic heating processes are also included. The transport equation is solved in log-space, with speed bins ranging from 1 to 6200 km s^{-1} (or ∼0.5 eV–200 keV). The bin size is constant in log-space, ranging from 1 to 44 km s^{-1} in linear space. For the previous results in Sections 3.1 and 3.2, we assumed that the energy diffusion term $D = 0$. Here, we allow it to be nonzero, with the same form as used by Zirnstein et al. (2025). A summary of the methodology is given in the Appendix.

The mechanism for particle energy diffusion in the HS is not well-established, but it has been shown that a mixture of Alfvénic and compressible turbulence may be responsible for the energization of PUIs in the HS based on comparisons with IBEX-Lo and IBEX-Hi observations (E. J. Zirnstein et al. 2018b). This turbulence may originate from the SW (S. V. Chalov et al. 2003), as well as from fluctuations from the termination shock itself. It is also possible that the energy diffusion of PUIs in the HS arises from statistical acceleration by transit-time damping from magnetic field magnitude variations in the HS, similar to what happens in the SW (N. A. Schwadron et al. 1996). Despite

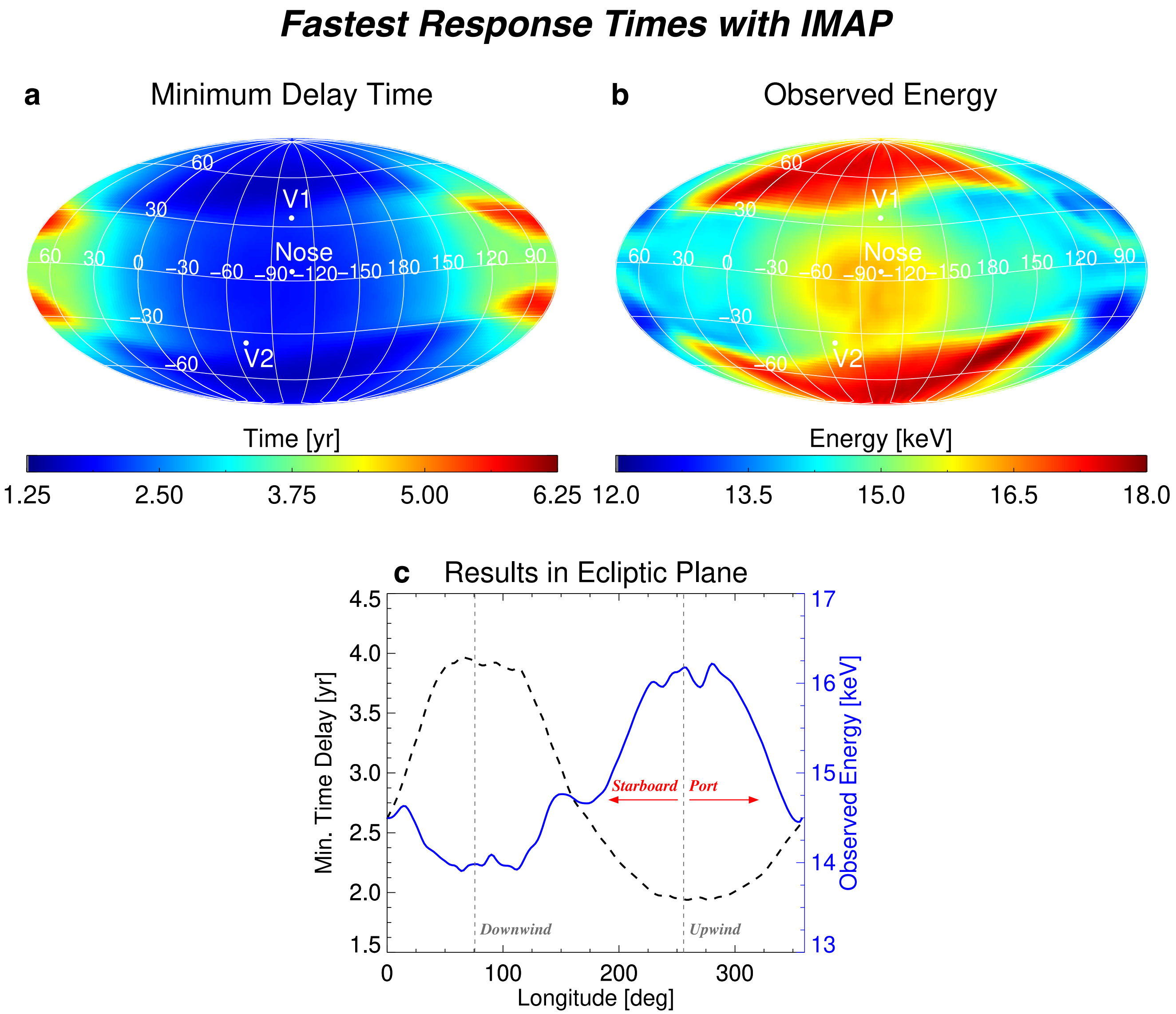

Figure 5. (a) Minimum delay (or quickest) time per pixel in the sky. (b) Energy at which the minimum delay time is observed. (c) Minimum delay time and the energy at which it is observed as a function of longitude along the ecliptic plane.

our lack of knowledge regarding its origin, this paper demonstrates how energy diffusion affects IMAP ENA emissions from the HS.

When we include energy diffusion, we assume that the turbulent fluctuations or waves cause particle diffusion decay with distance along the MHD plasma flow streamlines. We use the exponential function, exp($-s/\lambda_{\mathrm{D}}$), where s is the streamline distance from the termination shock and λ_{D} is the mean free path. This function is multiplied to the diffusion coefficient amplitude. In Figures 9 and 10, we show results for $\lambda_{\mathrm{D}} = 0$ ("No Diffusion"), $\lambda_{\mathrm{D}} = 200$ au, and $\lambda_{\mathrm{D}} = 2000$ au. These values are chosen arbitrarily, but they allow us to explore the effects of energy diffusion when the mean free path of decay is vastly different over scale sizes similar to the termination shock ($\lambda_{\mathrm{D}} = 200$ au) and the heliosphere ($\lambda_{\mathrm{D}} = 2000$ au).

Figure 9 shows the mean SW-to-ENA time delay from the port direction of the heliosphere. We choose this direction because the lengths of flow streamlines intersecting the LOS vary over hundreds of au. As one can see, with the inclusion of energy diffusion, the time delay has increased over all energies, indicating the ENA source distribution in the HS has increased to greater distances from the termination shock. The mean standard error has also increased due to the wider spread in ENA source region. Finally, the minimum SW-to-ENA time delay over all energies has increased to ∼20–30 keV ($\lambda_{\mathrm{D}} = 200$ au) and ∼30–40 keV ($\lambda_{\mathrm{D}} = 2000$ au), because the response time at higher energies in the IMAP-Ultra regime has not increased as much as at lower energies. The difference between no diffusion and some diffusion is significant, depending on the amplitude, which is also illustrated in Figure 10.

Figure 10 shows meridional cross sections (for brevity, we do not show equatorial cross sections, but they reveal similar results) through the simulated heliosphere of the local ENA source distribution. Note that each row shows one example of an energy passband/bin for IMAP-Lo (top), IMAP-Hi (middle), and IMAP-Ultra (bottom). The cases for different diffusion amplitudes (or different mean free path λ_{D}) are shown in three columns. The column with "No Diffusion" displays the same results as shown earlier in Figures 6–8, but note that the color bar ranges have changed. For IMAP-Lo

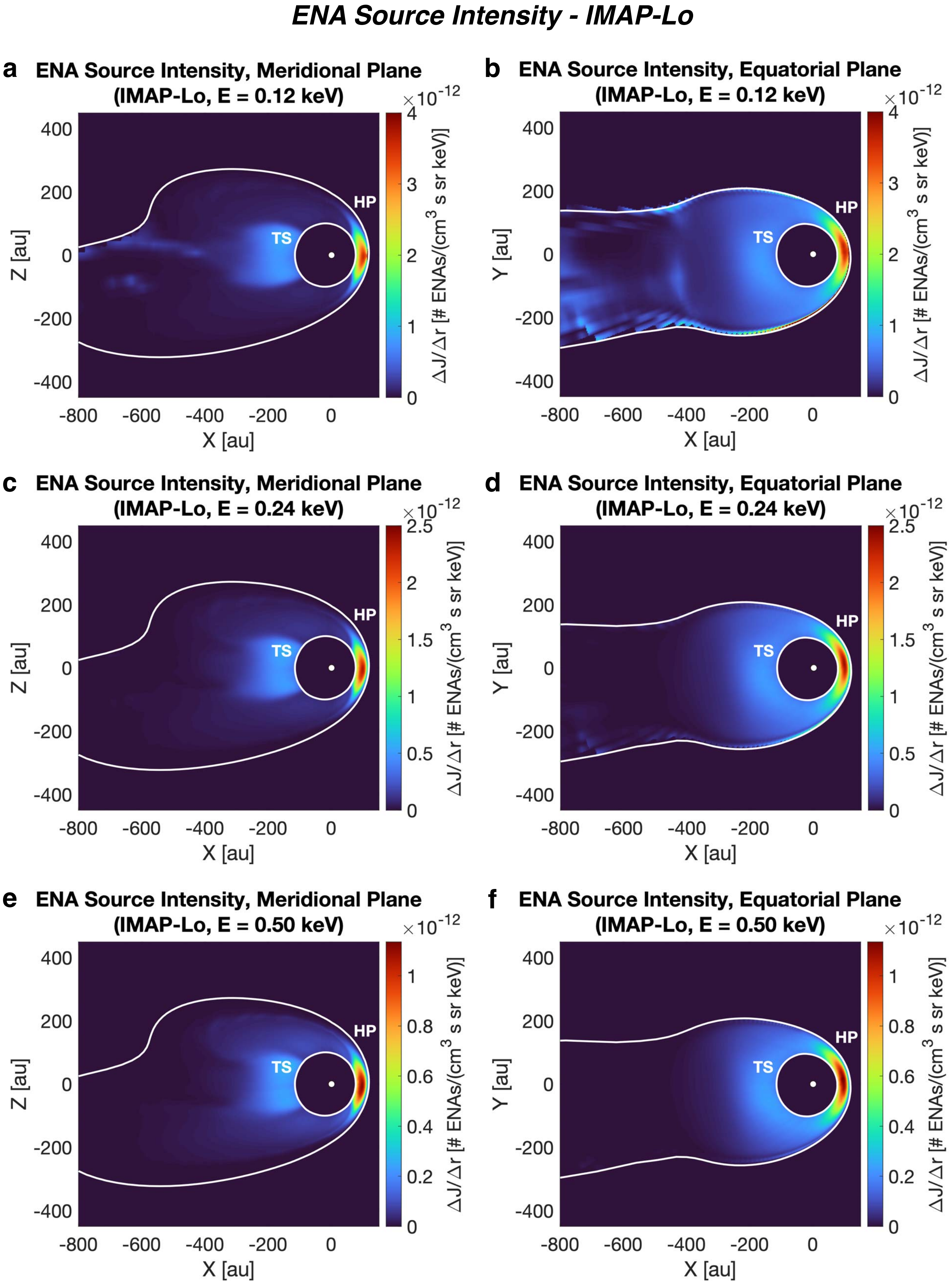

Figure 6. ENA source intensity ($\Delta J/\Delta r$) for IMAP-Lo energies in (panels (a), (c), and (e)) meridional and (panels (b), (d), and (f)) equatorial cuts through the simulated heliosphere. The TS and HP boundaries are shown as white contours. During the calculation of ENA production, the HP is defined by a temperature iso-surface at $\sim 10^5$ K. Moreover, within this iso-surface, ENA production is only allowed if the local MHD flow streamline connects back to the Sun.

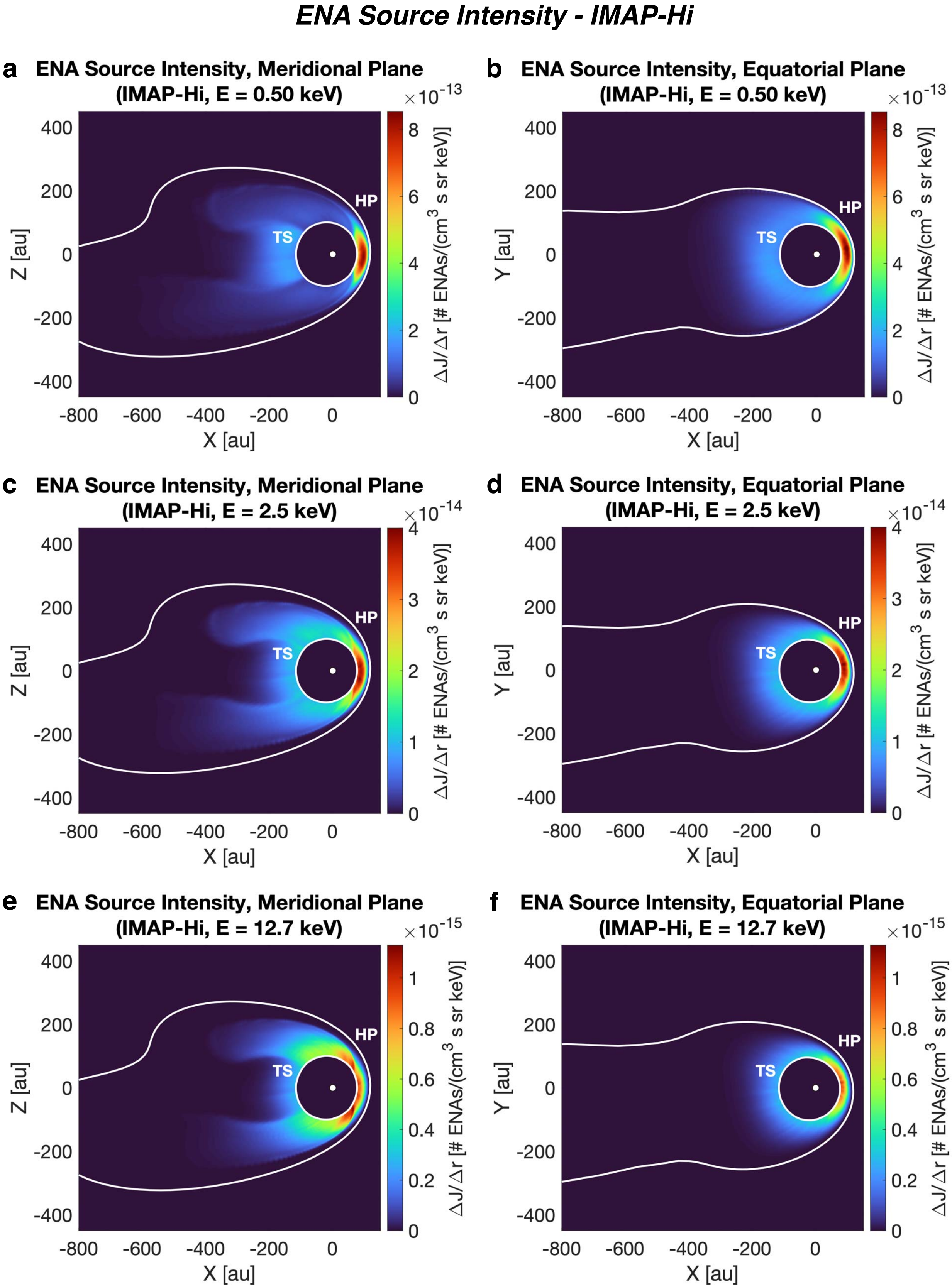

Figure 7. Same as Figure 6, except for IMAP-Hi energies.

energies, when diffusion is included, the ENA source distribution increases farther down the central tail, as well as along the inner surface of the heliopause. This becomes more pronounced for larger λ_D. This is because diffusion effectively moves "core" particles to higher energies, leading to more ENAs. For IMAP-Hi, the increase in energy diffusion increases

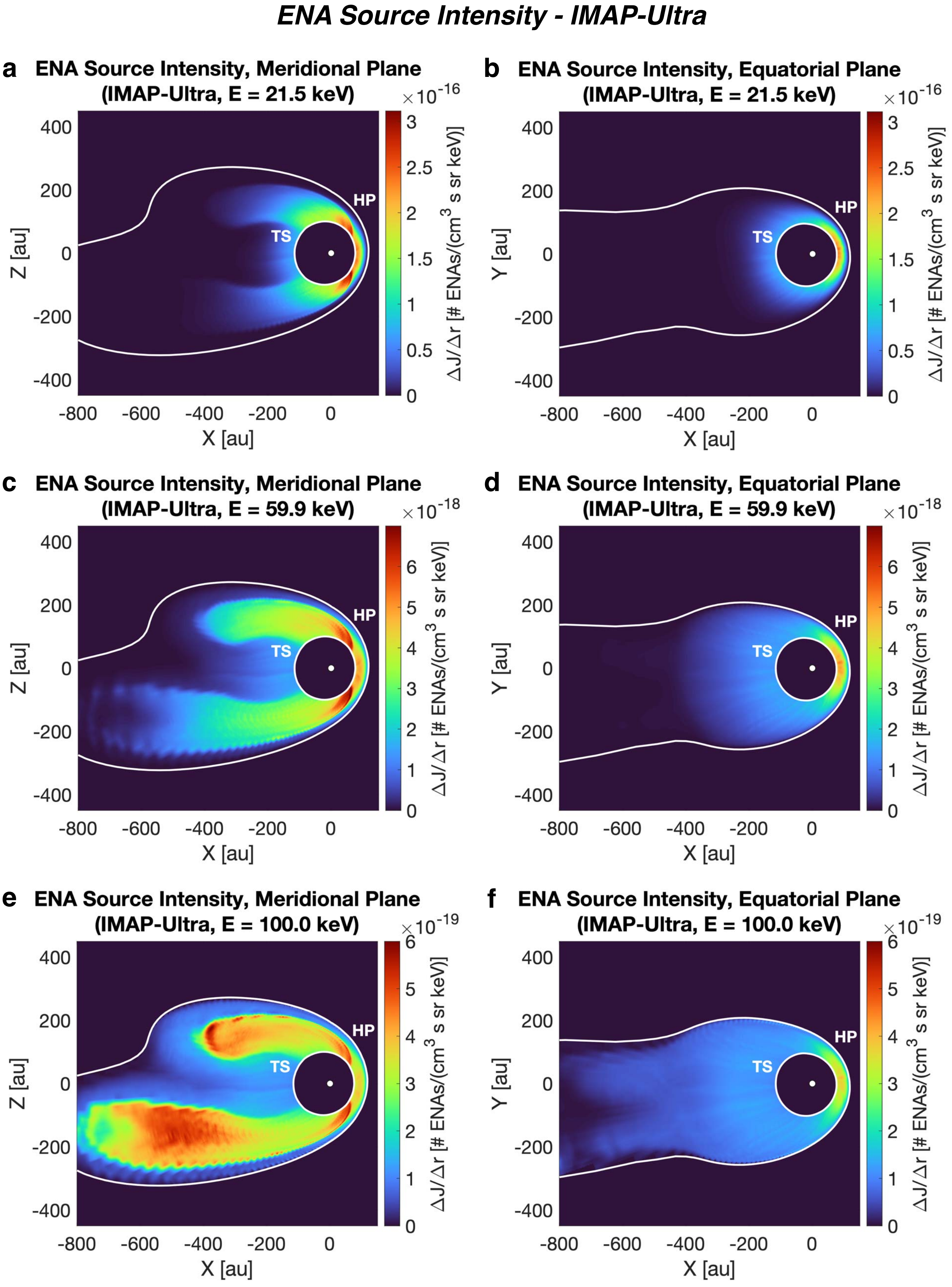

Figure 8. Same as Figure 6, except for IMAP-Ultra energies.

the ENA source distribution in the high-latitude, fast-SW regions of the heliotail, as well as the front of the heliosphere centered near the nose. Both IMAP-Lo and IMAP-Hi results show this increase near the nose. For IMAP-Ultra, the differences are more subtle (note that the change in ENA production is more pronounced than the location of the ENA

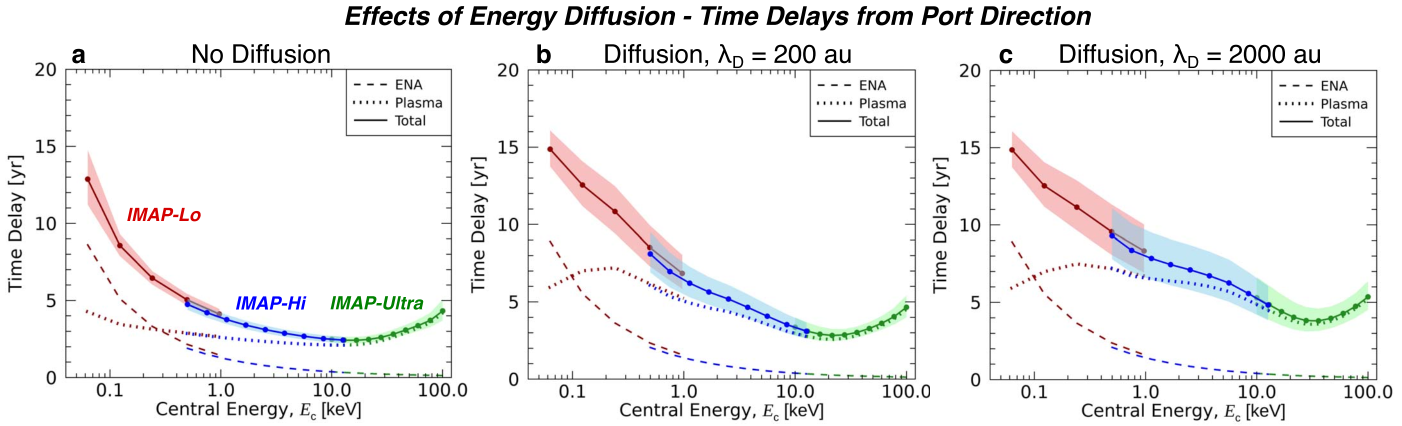

Figure 9. Time delays from the port direction (a) without energy diffusion, (b) with diffusion whose diffusion coefficient amplitude D decays as exp(-s/λ_D), where s is the streamline distance from the termination shock and $\lambda_D = 200$ au. Panel (c) is the same as panel (b), except $\lambda_D = 2000$ au.

source distribution). The ENA source distribution far back in the tail slightly increases in the fast/hot-SW lobes out to $x = -800$ au. Diffusion has only slightly increased the ENA intensity near the nose. These results show the unique energy-dependent relationship between the ENA source intensity and parent proton energy diffusion process in the HS.

4. Discussion and Conclusions

Motivated by the upcoming launch of the IMAP mission in 2025, as well as the dynamic variability that ENA emissions from the HS have shown over the past solar ~16 yr of IBEX-Hi observations, we present simulation results of the ENA emissions expected to be measured by IMAP-Lo, IMAP-Hi, and IMAP-Ultra, spanning an energy range of $\lesssim$0.1 keV to >100 keV (D. J. McComas et al. 2018a). We utilized a global MHD-plasma/kinetic-neutral simulation of the heliosphere to compute ENA emissions, their source distributions as a function of space and instrument energy passband/bin, and the SW-to-ENA time delays in different directions of the sky. The intent is to understand how large, global changes in the SW may be viewed over time by the IMAP ENA imagers as a function of energy. We focused here on time delays and relative ENA source distribution, rather than the total ENA flux observable at 1 au, due to the current lack of understanding energy diffusion in the HS. We hope that, in the near future, with better theoretical/numerical and observational analyses to study this key physical process, we can better understand the ENA source distribution and constrain the diffusion coefficient in the HS, as was done in one direction of the sky by E. J. Zirnstein et al. (2018b, 2018c) using IBEX-Lo (S. A. Fuselier et al. 2009) and IBEX-Hi data. We note that including energy diffusion in the HS has the potential to at least partially solve the "ENA gap" problem between most ENA models and observations (E. J. Zirnstein et al. 2017; M. Kornbleuth et al. 2018, 2021; I. I. Baliukin et al. 2020, 2022; M. Gkioulidou et al. 2022), although part of the discrepancy can partly be explained by preferential PUI acceleration at the termination shock (E. J. Zirnstein et al. 2021, 2022a, 2024; R. K. Bera et al. 2023; M. Kornbleuth et al. 2023; B. Wang et al. 2023). We note that energy diffusion in the HS has also been demonstrated to reasonably improve the comparison between one ENA model and IBEX data (E. J. Zirnstein et al. 2025), but more work is likely needed to refine our understanding of diffusion in the HS. In this study, we demonstrate a potential energy diffusion process that decays with distance from the termination shock, which clearly increases ENA emissions over most IMAP ENA energies.

Using current information about the IMAP ENA imagers' energy passband/bin information (Table 1), we simulated the SW-to-ENA time delay for various directions in the sky. We see asymmetries in the upwind versus downwind, port versus starboard, and north versus south pole directions, largely influenced by the (1) nose versus tail structure as our heliosphere moves through interstellar space and (2) the interstellar magnetic field draped around the heliosphere breaking the cylindrical symmetry of the heliosphere (as well as the fast SW at high latitudes breaking the symmetry). We find that, at energies (without energy diffusion) around ~15 keV, the response time is the quickest at <2 yr, but at the lowest and highest energies of the IMAP-Lo and IMAP-Ultra energy ranges, the response time to global changes in the SW can be seen later. When energy diffusion is included, we find this energy range increases to at least ~40 keV. This implies that the highest-energy passband of IMAP-Hi (FWHM range from ~10 to 15 keV) and the lower-energy bins of IMAP-Ultra (from ~10 to 40 keV) and their overlap from near 15 keV should be particular foci of research once IMAP ENA observations are collected. Global SW events such as the abrupt increase in SW dynamic pressure in late 2014, for example, are prime candidate events to study with overlapping IMAP-Hi and IMAP-Ultra energies. This also implies we can improve our understanding of the shape—and potentially the dynamic structure—of the heliosphere (D. B. Reisenfeld et al. 2021) via IBEX ENA observations with IMAP's improved capabilities.

The time delay does not behave monotonically with energy, due to the H+p charge-exchange cross section (affecting high energies), but also because of the relative time it takes for the outbound SW plasma and inbound ENAs to travel such large distances as a function of ENA energy (affecting both high and low energies) (Figure 3). It is possible that measurements of ENAs at the lowest energies near ~0.1 keV and highest energies above ~60 keV can view ENA emission sources the farthest down the heliosphere (see also M. Kornbleuth et al. 2023), although the "wait" time to view global changes at low energies is significantly longer, such that making any correlations with changes in the SW becomes nearly impossible. However, at energies >60 keV, the delay is not significantly longer, even when energy diffusion is included. For this reason, we expect

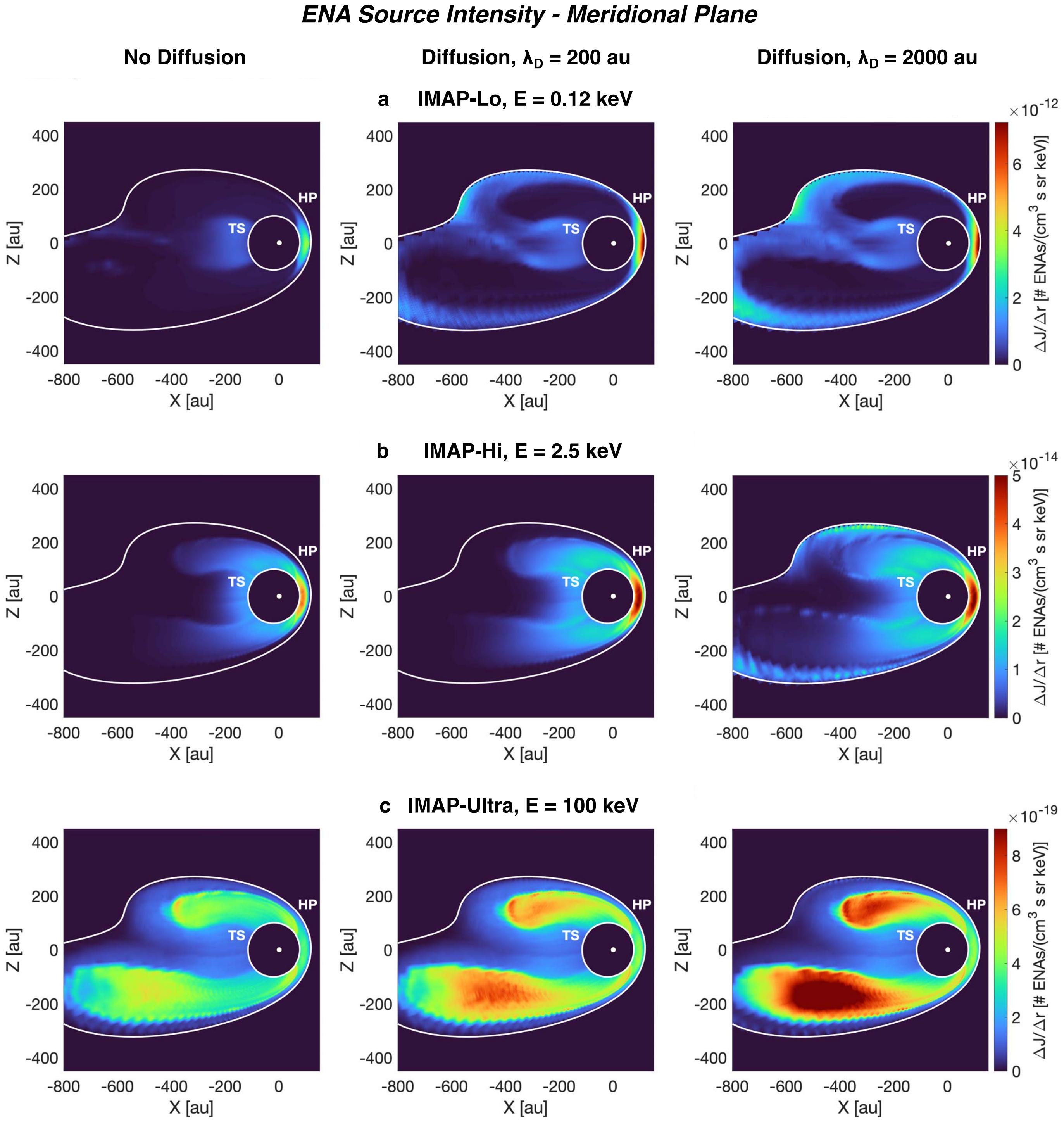

Figure 10. Example ENA source distributions for each IMAP ENA imager (panels (a)–(c)) without energy diffusion (left column), and with diffusion (middle and right columns).

IMAP-Ultra to provide new insights into the workings of the distant outer heliosphere.

We show that, by including the effects of energy diffusion in our model, the spatial ENA source distribution can change dramatically, depending on the ENA energy and the mean free path for the decay of diffusion. For example, at $E_c = 0.12$ keV, energy diffusion increases the ENA emission rate at low latitudes but also near the heliopause where the plasma temperature is colder and diffusion helps accelerate some protons to higher energies. At $E_c = 2.5$ keV, ENA emissions in the central tail are slightly increased, but the biggest differences occur in regions where the SW originated from the polar coronal holes (PCHs). While our simulation of the heliosphere is in a steady state with solar minimum-like conditions, the increase in ENA emissions will likely follow the solar cycle. In the future, we will apply our ENA model to a time-dependent simulation of the heliosphere that has solar cycle effects, in particular with the opening and closing of the PCHs (N. V. Pogorelov et al. 2013; E. J. Zirnstein et al. 2017; F. Fraternale et al. 2024). Finally, at $E_c = 100$ keV, there is a moderate increase in ENA intensity, in particular in the heliotail's fast/hot SW regions. Depending on the local amplitude of the diffusion, it may slightly shorten the distance over which we can observe ENAs coming from, or it may lengthen it. As demonstrated here, the higher-energy measurements from IMAP-Ultra should provide a "deeper" view down the heliotail compared to lower energies, without a significant delay in time (except in directions near the central heliotail, where the wait time can be >20 yr). We note, however, that it is unclear what the true SNR will be near ∼100 keV, where the number of counts may be too low to calculate a meaningful intensity. Therefore, our results near ∼100 keV for IMAP-Ultra should be interpreted with this in mind.

IMAP, with its enhanced ENA imager capabilities compared to its predecessors (D. J. McComas et al. 2018a), will help us better constrain the minimum distance to the ENA source in the heliotail, as well as the diffusion rate, which can affect the observed ENA intensities.

Acknowledgments

We gratefully acknowledge the efforts of the IMAP team in making this mission possible. This work was funded by the IBEX mission as a part of NASA's Explorer Program (grant No. 80NSSC20K0719) and the IMAP mission as a part of NASA's Solar Terrestrial Probes mission line (grant No. 80GSFC19C0027). E.J.Z. also acknowledges partial support from NASA grant No. 80NSSC24K0267 under subaward 2024–1824. E.J.Z. thanks George Livadiotis for helpful discussions. The simulations reported in this paper were performed at the TIGRESS high-performance computer center at Princeton University, which is jointly supported by the Princeton Institute for Computational Science and Engineering and the Princeton University Office of Information Technology's Research Computing department.

Appendix

The ENA source distribution is calculated from the charge-exchange conversion from HS protons. The distribution of protons is calculated as a function of position in the HS by solving the Parker transport equation with advection, energy diffusion (assuming $D = 0$ and $D > 0$), adiabatic heating, and production/loss source terms. We solve the Parker transport equation in log-space for computational efficiency, using the finite difference method. The transport equation is given as

$$\begin{aligned} f_j^{n+1} = {} & f_j^n + \frac{\Delta s e^{-3w_j}}{u_p \Delta w^2}\left[D_{j+\frac{1}{2}} e^{w_{j+\frac{1}{2}}}(f_{j+1}^n - f_j^n)\right. \\ & \left. - D_{j-\frac{1}{2}} e^{w_{j-\frac{1}{2}}}(f_j^n - f_{j-1}^n)\right] + \frac{\Delta s}{3u_p}(\nabla \cdot \boldsymbol{u}_p) \\ & \times \left[\frac{f_{j+1}^n - f_{j-1}^n}{2\Delta w}\right] + \frac{\Delta s}{u_p}[\eta_j^n f_{H,j}^n - \beta_j^n f_j^n], \end{aligned} \tag{13}$$

where f is the proton distribution function, n represents the time step, j is the speed bin, the second term on the right-hand side is energy diffusion, the third term is adiabatic heating due to flow divergence, and the last term in brackets contains the production ($\eta_j^n f_{H,j}^n$) and loss ($\beta_j^n f_j^n$) source terms (where $f_{H,j}^n$ is the local neutral H distribution from the simulation, which we assume is Maxwellian for simplicity). The variable $w = \ln(v)$, Δs is the step size in space (and also effectively in time), and u_p is the local MHD plasma flow speed. The diffusion coefficient is represented as $D(v) = D_0 v^{\alpha}$, where D_0 is the amplitude, v is the particle speed, and $\alpha = 1.31$ is the spectral index derived from chi-square minimization of fitting to IBEX-Lo and IBEX-Hi data (E. J. Zirnstein et al. 2018b, 2025).

The diffusion amplitude D_0 is replaced as a direction and positional dependent parameter. First, it is scaled with the time it takes the SW to reach the termination shock, $\tau(\Omega_{\mathrm{TS}})$, where we replace D_0 with variable $D_0'(\Omega_{\mathrm{TS}})$ given as

$$D_0'(\Omega_{\mathrm{TS}}) = D_0(\tau_{\mathrm{tail,ref}}/\tau(\Omega_{\mathrm{TS}}))^{2.5}, \tag{14}$$

where Ω_{TS} is the direction in the sky to the termination shock (TS), $\tau_{\mathrm{tail,ref}} = 1.34$ yr is the reference mean time originally derived by E. J. Zirnstein et al. (2018b) from just the central tail direction in an older simulation of the heliosphere, and $\tau(\Omega)$ is the time computed in the current heliosphere simulation. The power exponent of 2.5 is derived from the work of G. P. Zank et al. (1996). More details can be found in E. J. Zirnstein et al. (2025).

The diffusion amplitude in Equation (3) is further modified in this study to account for an exponential decline in energy diffusion with distance along the bulk plasma flow streamlines. We choose an exponential function to represent this decline, mostly for simplicity, but the rate of decline may be more complex depending on the type of turbulence that exists in the HS, such as SW turbulence advected across the termination shock (S. V. Chalov et al. 2003; J. Giacalone et al. 2021), or perhaps instabilities that develop in the heliotail (S. N. Borovikov et al. 2008; M. Opher et al. 2015, 2020; F. Fraternale et al. 2024). This unknown is why we show two different results for the mean free path of the diffusion: $\lambda_D = 200$ au and 2000 au. Note that we tested a linear decrease where diffusion reaches zero at a streamline distance of 500 au from the termination shock, and the results are very similar to the case of exponential decrease with $\lambda_{\mathrm{D}} = 200$ au. Therefore, we believe an exponential decline is a reasonable function to use for this demonstration.

Using the exponential decline in diffusion along streamlines, $D(v)$ can now be written as

$$D(v, s, \Omega_{\mathrm{TS}}) = D_0 v^{\alpha}(\tau_{\mathrm{tail,ref}}/\tau(\Omega_{\mathrm{TS}}))^{2.5}\exp(-s/\lambda_D). \tag{15}$$

ORCID iDs

E. J. Zirnstein https://orcid.org/0000-0001-7240-0618
J. Heerikhuisen https://orcid.org/0000-0001-7867-3633
D. J. McComas https://orcid.org/0000-0001-6160-1158
M. A. Dayeh https://orcid.org/0000-0001-9323-1200
H. O. Funsten https://orcid.org/0000-0002-6817-1039
M. Gkioulidou https://orcid.org/0000-0001-9979-2164
D. G. Mitchell https://orcid.org/0000-0003-1960-2119
D. B. Reisenfeld https://orcid.org/0000-0003-1874-9450
N. A. Schwadron https://orcid.org/0000-0002-3737-9283

References

Baliukin, I. I., Izmodenov, V. V., & Alexashov, D. B. 2020, MNRAS, 499, 441
Baliukin, I. I., Izmodenov, V. V., & Alexashov, D. B. 2022, MNRAS, 509, 5437
Baranov, V. B., & Malama, Y. G. 1993, JGR, 98, 15157
Barnett, C. F., Hunter, H. T., Fitzpatrick, M. I., et al. 1990, STIN, 91, 13238
Bera, R. K., Fraternale, F., Pogorelov, N. V., et al. 2023, ApJ, 954, 147
Borovikov, S. N., Pogorelov, N. V., Zank, G. P., & Kryukov, I. A. 2008, ApJ, 682, 1404
Burlaga, L. F., Berdichevsky, D. B., Jian, L. K., et al. 2021, ApJ, 906, 119

Burlaga, L. F., Ness, N. F., Acuña, M. H., et al. 2008, Natur, 454, 75
Burlaga, L. F., Ness, N. F., Berdichevsky, D. B., et al. 2019, NatAs, 3, 1007
Burlaga, L. F., Ness, N. F., & Stone, E. C. 2013, Sci, 341, 147
Bzowski, M., Czechowski, A., Frisch, P. C., et al. 2019, ApJ, 882, 60
Bzowski, M., & Heerikhuisen, J. 2020, ApJ, 888, 24
Chalov, S. V., Fahr, H. J., & Izmodenov, V. V. 2003, JGRA, 108, 1266
Dialynas, K., Krimigis, S. M., Decker, R. B., et al. 2022, SSRv, 218, 21
Fraternale, F., Pogorelov, N. V., & Bera, R. K. 2024, ApJL, 974, L15
Funsten, H. O., Allegrini, F., Bochsler, P., et al. 2009, SSRv, 146, 75
Fuselier, S. A., Bochsler, P., Chornay, D., et al. 2009, SSRv, 146, 117
Galli, A., Baliukin, I. I., Bzowski, M., et al. 2022, SSRv, 218, 31
Galli, A., Wurz, P., Schwadron, N. A., et al. 2017, ApJ, 851, 2
Giacalone, J., Nakanotani, M., Zank, G. P., et al. 2021, ApJ, 911, 27
Gkioulidou, M., Opher, M., Kornbleuth, M., et al. 2022, ApJL, 931, L21
Gurnett, D. A., Kurth, W. S., Burlaga, L. F., & Ness, N. F. 2013, Sci, 341, 1489
Heerikhuisen, J., Florinski, V., & Zank, G. P. 2006, JGRA, 111, A06110
Heerikhuisen, J., & Pogorelov, N. V. 2010, in ASP Conf. Ser. 429, Numerical Modeling of Space Plasma Flows: ASTRONUM 2009, ed. N. V. Pogorelov, E. Audit, & G. P. Zank (San Francisco, CA: ASP), 227
Heerikhuisen, J., Zirnstein, E. J., Funsten, H. O., Pogorelov, N. V., & Zank, G. P. 2014, ApJ, 784, 73
Kornbleuth, M., Opher, M., Baliukin, I., et al. 2021, ApJ, 921, 164
Kornbleuth, M., Opher, M., Dialynas, K., et al. 2023, ApJL, 945, L15
Kornbleuth, M., Opher, M., Michael, A. T., & Drake, J. F. 2018, ApJ, 865, 84
Krimigis, S. M., Decker, R. B., Roelof, E. C., et al. 2019, NatAs, 3, 997
Lindsay, B. G., & Stebbings, R. F. 2005, JGR, 110, A12213
McComas, D., Allegrini, F., Bagenal, F., et al. 2008, SSRv, 140, 261
McComas, D. J., Alexashov, D., Bzowski, M., et al. 2012, Sci, 336, 1291
McComas, D. J., Alimaganbetov, M., Beesley, L. J., et al. 2024, ApJS, 270, 17
McComas, D. J., Allegrini, F., Bochsler, P., et al. 2009a, Sci, 326, 959
McComas, D. J., Allegrini, F., Bochsler, P., et al. 2009b, SSRv, 146, 11
McComas, D. J., Bzowski, M., Dayeh, M. A., et al. 2020, ApJS, 248, 26
McComas, D. J., Bzowski, M., Fuselier, S. A., et al. 2015, ApJS, 220, 22
McComas, D. J., Christian, E. R., Schwadron, N. A., et al. 2018a, SSRv, 214, 116
McComas, D. J., Dayeh, M. A., Funsten, H. O., Livadiotis, G., & Schwadron, N. A. 2013, ApJ, 771, 77
McComas, D. J., Dayeh, M. A., Funsten, H. O., et al. 2018b, ApJL, 856, L10
McComas, D. J., Dayeh, M. A., Funsten, H. O., et al. 2019, ApJ, 872, 127
McComas, D. J., Zirnstein, E. J., Bzowski, M., et al. 2017, ApJS, 229, 41
Möbius, E., Bochsler, P., Bzowski, M., et al. 2009, Sci, 326, 969
Opher, M., Drake, J. F., Zieger, B., & Gombosi, T. I. 2015, ApJL, 800, L28
Opher, M., Loeb, A., Drake, J., & Toth, G. 2020, NatAs, 4, 675
Parker, E. N. 1961, ApJ, 134, 20
Pogorelov, N. V., Suess, S. T., Borovikov, S. N., et al. 2013, ApJ, 772, 2
Rankin, J. S., McComas, D. J., Richardson, J. D., & Schwadron, N. A. 2019, ApJ, 883, 101
Reisenfeld, D. B., Bzowski, M., Funsten, H. O., et al. 2021, ApJS, 254, 40
Richardson, J. D., Belcher, J. W., Garcia-Galindo, P., & Burlaga, L. F. 2019, NatAs, 3, 1019
Richardson, J. D., Wang, C., Liu, Y. D., et al. 2017, ApJ, 834, 190
Scherer, K., Fichtner, H., Fahr, H.-J., Bzowski, M., & Ferreira, S. E. S. 2014, A&A, 563, A69
Schwadron, N. A., Allegrini, F., Bzowski, M., et al. 2011, ApJ, 731, 56
Schwadron, N. A., Allegrini, F., Bzowski, M., et al. 2018, ApJS, 239, 1
Schwadron, N. A., Fisk, L. A., & Gloeckler, G. 1996, GeoRL, 23, 2871
Schwadron, N. A., Moebius, E., Fuselier, S. A., et al. 2014, ApJS, 215, 13
Sokół, J. M., Dayeh, M. A., Fuselier, S. A., et al. 2021, ApJ, 922, 250
Stone, E. C., Cummings, A. C., Heikkila, B. C., & Lal, N. 2019, NatAs, 3, 1013
Stone, E. C., Cummings, A. C., McDonald, F. B., et al. 2005, Sci, 309, 2017
Stone, E. C., Cummings, A. C., McDonald, F. B., et al. 2008, Natur, 454, 71
Stone, E. C., Cummings, A. C., McDonald, F. B., et al. 2013, Sci, 341, 150
Swaczyna, P., Bzowski, M., Dialynas, K., et al. 2024, ApJL, 969, L20
Swaczyna, P., McComas, D. J., Zirnstein, E. J., & Heerikhuisen, J. 2019, ApJ, 887, 223
Swaczyna, P., McComas, D. J., Zirnstein, E. J., et al. 2020, ApJ, 903, 48
Wang, B., Zank, G. P., Shrestha, B. L., Kornbleuth, M., & Opher, M. 2023, ApJ, 944, 198
Witte, M. 2004, A&A, 426, 835
Zank, G. P. 1999, SSRv, 89, 413
Zank, G. P. 2015, ARA&A, 53, 449
Zank, G. P., Heerikhuisen, J., Wood, B. E., et al. 2013, ApJ, 763, 20
Zank, G. P., Matthaeus, W. H., & Smith, C. W. 1996, JGR, 101, 17093
Zirnstein, E. J., Dayeh, M. A., McComas, D. J., & Sokół, J. M. 2020a, ApJ, 894, 13
Zirnstein, E. J., Dayeh, M. A., McComas, D. J., & Sokół, J. M. 2020b, ApJ, 897, 138
Zirnstein, E. J., Heerikhuisen, J., Funsten, H. O., et al. 2016, ApJL, 818, L18
Zirnstein, E. J., Heerikhuisen, J., McComas, D. J., et al. 2018a, ApJ, 859, 104
Zirnstein, E. J., Heerikhuisen, J., Pogorelov, N. V., McComas, D. J., & Dayeh, M. A. 2015, ApJ, 804, 5
Zirnstein, E. J., Heerikhuisen, J., Zank, G. P., et al. 2017, ApJ, 836, 238
Zirnstein, E. J., Kim, T. K., Dayeh, M. A., et al. 2022a, ApJL, 937, L38
Zirnstein, E. J., Kim, T. K., Rankin, J. S., et al. 2024, ApJ, 974, 213
Zirnstein, E. J., Kumar, R., Bandyopadhyay, R., et al. 2021, ApJL, 916, L21
Zirnstein, E. J., Kumar, R., Heerikhuisen, J., McComas, D. J., & Galli, A. 2018b, ApJ, 860, 170
Zirnstein, E. J., Kumar, R., Heerikhuisen, J., McComas, D. J., & Galli, A. 2018c, ApJ, 865, 150
Zirnstein, E. J., Kumar, R., Shrestha, B. L., et al. 2025, NatAs, in press
Zirnstein, E. J., & McComas, D. J. 2015, ApJ, 815, 31
Zirnstein, E. J., Shrestha, B. L., McComas, D. J., et al. 2022b, NatAs, 6, 1398